19th Brazilian Congress of Thermal Sciences and Engineering
November 6th–10th, 2022, Bento Gonçalves - RS - Brazil

ENC-2022-0046
NUMERICAL INFLUENCE OF VISCOUS FLUX CALCULATION SCHEMES FOR TURBULENT FLOW SIMULATIONS IN AERONAUTICAL APPLICATIONS

Thamires das Chagas Silva
Marco Aurélio Leonel Matunaga
Instituto Tecnológico de Aeronáutica, DCTA/ITA, 12228-900, São José dos Campos, SP, Brasil
th.daschagas@gmail.com, marco.matunaga@gmail.com

Ricardo Galdino da Silva
João Luiz F. Azevedo
Instituto de Aeronáutica e Espaço, DCTA/IAE/ALA, 12228-904, São José dos Campos, SP, Brasil
ri_galdino@yahoo.com.br, joaoluiz.azevedo@gmail.com

Abstract. *The present work is part of an ongoing effort to provide continuous improvement to an in-house developed CFD solver, known as BRU3D. This code is currently being used to simulate turbulent flows over realistic aeronautical and aerospace configurations. The BRU3D code is a cell-centered, finite volume code that solves the 3-D Reynolds-averaged Navier-Stokes (RANS) equations, together with appropriate turbulence closure models, using unstructured meshes. An upwind spatial discretization is adopted, together with terms that ensure the satisfaction of an entropy inequality in the artifical dissipation terms, and it has an implicit time marching. For cell-centered methods, the schemes to constructing of the inviscid fluxes in the interface cells are well explored by the CFD community, such that robust schemes are reported by the literature. However, the construction of gradients for the calculation of viscous fluxes is a matter that still requires community attention. These schemes impact on numerical robustness and in the final result of the simulation. The emphasis of the present effort is in the analysis of the influence of two different schemes for the definition of viscous gradient values at cell interfaces in the turbulent flow simulations of interest to the institutions represented here. The simulations are performed for flows that present complex physical phenomena, such as interaction between shock wave and boundary layer, and cases which might exhibit separation of the flow, even at lower angles of attack, which address multiple element airfoils typical of high lift configurations. Therefore, after some initial validation for standard configurations, the paper discuss results for transonic flow over the OAT15A airfoil and for high-lift flow over the McDonnell Douglas 30P30N multi-element airfoil. It will be seen that the influence of different schemes for the definition of viscous gradient values at cell interfaces is significant, demonstrating how much an accurate solution depends on numerical methods implemented in the code, not just the physics contained in the governing equations discretized by these methods.*

Keywords: *Computational Fluid Dynamics, Turbulent Flows, Navier-Stokes Equations, Flux Calculation Schemes.*

1. INTRODUCTION

External flows typical of the aerospace and aeronautic communities are usually turbulent flows, which the turbulence effects are very important for the solution. These flows are within the interests of the computational aerodynamic research group of Instituto de Aeronáutica e Espaço (IAE), in particular, the flows which are part of the daily practice of the industry. Nowadays, the Reynolds-averaged Navier-Stokes (RANS) formulation, together with appropriate turbulence modeling, is the main methodology used by the industry. This formulation can deal with three-dimensional, compressible viscous flows. The major drawback of the RANS methodology is to obtain a turbulence model to be able to represent with accuracy the complex physical phenomena present in the flows of the interest, such as boundary layer detachment due to the presence of adverse pressure gradient, the interaction between shock waves and boundary layer, the interaction between wakes and boundary layer, which are phenomena commonly present in aerospace and aeronautic flows. In general, the accuracy of a turbulence model is directly proportional to the complexity of its formulation. However, the governing equations, *i.e.*, in this case, the RANS formulation together with an adequate turbulence model, are not the single responsible factors for an accurate solution.

Numerical methods implemented in the computational code also influence the final solution. Calculation schemes for the definition of viscous flux gradients at cell interfaces are also important issues of interest to the present work. Nowadays, this is also an issue of the CFD community interest (Cary *et al.*, 2009; Carvalho *et al.*, 2018). Two schemes are used to understand the effect that different calculation forms of the viscous gradients have on the quality of the final solution, focusing on aeronautical applications. The work employed two turbulence models, the SST (Menter *et al.*, 2003) and the NLBSL-V2 (Hellsten, 2005) models, in order to observe the influence of different gradient calculation schemes on such models.

This paper is divided into four sections. The first section presents the motivation and goals of this work, and in the second section the theoretical and numerical formulations are described. The results obtained are presented and discussed in the third section and, in the last section, conclusions and future investigations end this document.

2. THEORETICAL AND NUMERICAL FORMULATIONS

The flows of interest in the present work are modeled by the 3-D compressible Reynolds-averaged Navier-Stokes (RANS) equations, and these equations are solved together with an appropriate turbulence closure model. These governing equations are discretized by the Roe scheme, which is an upwind method. In order to advance the solution in time, an implicit time marching scheme is employed. Both discretizations in space and time procedures are detailed in (Bigarella and Azevedo, 2009). The present work uses two different turbulence models, named here as SST (Menter *et al.*, 2003) and NLBSL-V2 (Hellsten, 2005) models. In the next subsections, such formulations and methods are presented briefly.

2.1 Reynolds-Averaged Navier-Stokes Equations

The RANS equations, in Cartesian coordinates, can be written as (Bigarella and Azevedo, 2009)

$$\frac{\partial \mathbf{Q}}{\partial t} + \nabla \cdot (\mathbf{P}_e - \mathbf{P}_v) = 0, \tag{1}$$

on which $\mathbf{Q}$ is the vector of conserved properties, defined as

$$\mathbf{Q} = \left\{ \begin{array}{c} \rho \\ \rho u \\ \rho v \\ \rho w \\ e \\ \rho\tau_1 \\ \rho\tau_2 \end{array} \right\}. \tag{2}$$

Here, ρ is the local fluid density, u, v and w are the components of the velocity vector, $\mathbf{v}$, e is the total energy per unity of volume and τ_1 and τ_2 represent the turbulent properties given by the turbulence closure model adopted. For two turbulence models used in this paper, the two turbulent properties are the turbulent kinetic-energy, k, and the turbulent kinetic energy dissipation, ω. The inviscid and viscous flux vectors are represented, respectively, as

$$\mathbf{P}_e = \left\{ \begin{array}{c} \rho\mathbf{v} \\ \rho u\mathbf{v} + p\hat{\imath}_x \\ \rho v\mathbf{v} + p\hat{\imath}_y \\ \rho w\mathbf{v} + p\hat{\imath}_z \\ (e+p)\mathbf{v} \\ \rho\tau_1\mathbf{v} \\ \rho\tau_2\mathbf{v} \end{array} \right\}, \qquad \mathbf{P}_v = \left\{ \begin{array}{c} 0 \\ (\tau_{xj} + \tau^t_{xj})\ \hat{\imath}_j \\ (\tau_{yj} + \tau^t_{yj})\ \hat{\imath}_j \\ (\tau_{zj} + \tau^t_{zj})\ \hat{\imath}_j \\ \beta_j\ \hat{\imath}_j \\ \mu_{diff_1}\tau_{1,j}\hat{\imath}_j \\ \mu_{diff_2}\tau_{2,j}\hat{\imath}_j \end{array} \right\}. \tag{3}$$

The shear-stress tensor, τ_{ij}, is defined as

$$\tau_{ij} = \mu_l \left[\left(\frac{\partial u_i}{\partial x_j} + \frac{\partial u_j}{\partial x_i} \right) - \frac{2}{3} \frac{\partial u_m}{\partial x_m} \delta_{ij} \right], \tag{4}$$

where μ_l is the molecular dynamic viscosity coefficient, determined by the Sutherland law (Blazek, 2015). The viscous force work and heat transfer term, β_j, is written how $\beta_j = \tau_{ji}u_i - q_j$, where the heat conduction vector is written as

$$q_j = -\gamma \left(\frac{\mu_l}{Pr} + \frac{\mu_t}{\mathrm{Pr}_t} \right) \frac{\partial(e_i)}{\partial x_j}, \tag{5}$$

where γ is the specific heat ratio of air, e_i is the internal energy and μ_t is the turbulent eddy viscosity. Usually, constant values are adopted for Prandtl and turbulent Prandtl numbers, being $Pr = 0.72$ and $Pr_t = 0.9$, respectively (Blazek,

2015). The dimensionless pressure, p, can be calculated by equation of state for a thermally and calorically perfect gas, in agreement with types of flows studied in this work.

The Reynolds stress tensor, τ_{ij}^t, which appears from Favre averaging procedure as $\tau_{ij}^t = -\overline{\rho u_i'' u_j''}$, and the turbulent eddy viscosity, μ_t, are modeled by an appropriate turbulence model. Through these terms, the turbulence effects are included in the RANS equations. In the next subsection, the two turbulence models used in this work are briefly described.

2.2 Turbulence Modeling

The turbulence modeling can be classified according to how the Reynolds stress tensor is computed. They are the linear eddy viscosity models, nonlinear eddy viscosity models and the Reynolds stress models. Such classification is arranged in ascending order of complexity of its formulation. So, in general, it is expected that the linear eddy viscosity models had a poorer representation of complex physical phenomena than nonlinear eddy viscosity models, and so on.

The first model here employed is the Shear Stress Transport (SST) model. It was originally developed by Menter (1994), but the version used in this study is reported by Menter *et al.* (2003). This is a two-equation eddy-viscosity turbulence model, so it is a linear closure since adopts the Boussinesq hypothesis, which writes τ_{ij}^t as

$$\tau_{ij}^t = 2\mu_t \left(S_{ij} - \frac{1}{3}\frac{\partial u_k}{\partial x_k}\delta_{ij} \right) - \frac{2}{3}\rho k \delta_{ij} \ , \qquad S_{ij} = \frac{1}{2}\left(\frac{\partial u_i}{\partial x_j} + \frac{\partial u_j}{\partial x_i} \right) \ . \tag{6}$$

This approach links the Reynolds stress tensor to the mean strain rate tensor through the turbulent eddy viscosity, μ_t. This hypothesis results in some limitations, one which stands out is the poor representation of the Reynolds stress transport and another issue is to assume the isotropy of normal stresses for the Reynolds stress tensor. To overcome the first limitation, the SST model redefined the turbulent eddy viscosity in a way to take into account the effect of the transport of the principal turbulent shear stress (Menter, 1994). This improved the prediction of adverse pressure gradient flows, but the second limitation can not be overcome with this methodology.

A way of considering the anisotropy of normal stress for the Reynolds stress tensor on an existing eddy viscosity model framework is through nonlinear turbulence models. In this approach, nonlinear relationships are included to calculate the Reynolds stress tensor and the turbulent eddy viscosity. So, the second turbulent model used in this work is the nonlinear model developed by Hellsten (2005) and Wallin and Johansson (2000). In this model, the Reynolds stress tensor and the turbulent eddy viscosity are given by

$$\tau_{ij}^t = 2\mu_t \left(S_{ij} - \frac{1}{3}\frac{\partial u_k}{\partial x_k}\delta_{ij} \right) - \frac{2}{3}\rho k \delta_{ij} - \rho k a_{ij}^{(ex)} \ , \qquad \mu_t = C_\mu^{eff} \rho k \tau \ . \tag{7}$$

Here, $a_{ij}^{(ex)}$ is the Reynolds stress anisotropy tensor and C_μ^{eff} is an effective coefficient calculated by the model. Through these terms, nonlinear relationships are included in the Reynolds stress tensor, enabling the anisotropy of normal stresses of τ_{ij}^t to be calculated and incorporating more advanced turbulence effects.

To improve the accuracy of this model in cases of compressible flows, a modification is made regarding the original version of Hellsten (2005) and Wallin and Johansson (2000). In the transport equation of ω, the production term is divided by μ_t (das Chagas Silva, 2021) instead of k/ω, as in the original version of this model. This modification is done with the aim of adding the most significant compressible effects to the model. This version of the nonlinear model is named here as NLBSL-V2.

2.3 Numerical Formulation

The RANS and turbulence model equations are solved in a cell-centered finite volume context, being written as

$$\frac{\partial \mathbf{Q}_i}{\partial t} = -\frac{1}{V_i}\sum_{k=1}^{nf} \left[\left(\mathbf{P}_{e_k} - \mathbf{P}_{v_k} \right) \cdot \mathbf{S}_k \right] \ . \tag{8}$$

Here, k subscript represents properties computed in the $k-$th face, nf is the total number of faces of the i-th control volume and $\mathbf{S}_k$ is the area vector of the k-th face. Equation (8) assumes constant fluxes through volume faces and constant $\mathbf{Q}_i$ properties inside of the i-th volume. Convective flux calculations are made by the Roe flux-difference splitting scheme (Roe, 1981). Hence, the inviscid flux through the k-th face can be written as

$$\mathbf{P}_{ek} \cdot \mathbf{S}_k = \frac{1}{2}\left[\mathbf{P}_e\left(\mathbf{Q}_L \right) + \mathbf{P}_e\left(\mathbf{Q}_R \right) \right] \cdot \mathbf{S}_k - \frac{1}{2}|\tilde{\mathbf{A}}_k| \left(\mathbf{Q}_R - \mathbf{Q}_L \right) |\mathbf{S}_k| \ , \tag{9}$$

which R and L subscripts indicate right and left cells to the k-th face, respectively, and $|\tilde{\mathbf{A}}_k|$ is the Roe matrix.

A linear reconstruction of the primitive properties at the control volume faces is performed using the MUSCL scheme (van Leer, 1979) in order to obtain the $k-$th face values. The primitive variables, namely $q = p, u, v, w, e_i, \tau_1, \tau_2$, are,

then, used to obtain the vector of conserved variables, $\mathbf{Q}$, given by Eq. (2) (Bigarella, 2007). This approach can be written as

$$(q_L)_k = q_i + \psi_i \nabla q_i \cdot \vec{r}_{ki} \ , \qquad (q_R)_k = q_m + \psi_m \nabla q_m \cdot \vec{r}_{km} \ , \tag{10}$$

where ∇q_i and ∇q_m are the gradients computed for the $i-$th volume and its neighboring $m-$th volume, respectively; ψ_i and ψ_m represent the limiter functions in these volumes, and $\vec{r}_{ki}$ and $\vec{r}_{km}$ are the distance vectors between the $k-$th face centroid and $i-$th and $m-$th volume centroids, respectively.

In regions where the flow field contains strong gradients, the limiter function should be used in order to prevent non-physical oscillations of the solution (Blazek, 2015). For instance, at strong discontinuities, like shock waves, the limiter function reduces the slopes to interpolate the flow variables to the face of a control volume to constraint the solution variations. The first limiter function for unstructured mesh was implemented by Barth and Jespersen (1989) (Blazek, 2015). Its formulation bounded the extrapolated property in the $k-$th face of the $i-$th volume by the maximum and minimum values over the $i-$th volume centroid and its neighboring volume centroids. This can be mathematically expressed as

$$q_i^- \leq (q_i)_k \leq q_i^+ \ , \tag{11}$$

where

$$q_i^- = \min_{\mathrm{m}}(q_i, q_m) \ , \qquad q_i^+ = \max_{\mathrm{m}}(q_i, q_m) \ , \tag{12}$$

where m represents the index of all adjacent volumes that share a face with the $i-$th volume. This work uses the van Albada limiter function (Bigarella and Azevedo, 2005), which is based on the work of Barth and Jespersen (1989). The details of the van Albada limiter function extended for the multidimensional case, as employed here, are reported by Bigarella and Azevedo (2005).

While the schemes for construction of the inviscid flux in the volume faces are well explored by the CFD community in cell-centered methods, the schemes for construction of the viscous flux still require attention. Viscous flux calculations need the values of $\mathbf{Q}$ property gradients at the volume faces. Typically, in cell-centered methods, the gradients are computed as cell-averaged gradients and, then, extrapolated to cell faces. The schemes to perform these two procedures impact the numerical robustness (Jalali *et al.*, 2014; Cary *et al.*, 2009) and the final solution of the simulation (Carvalho *et al.*, 2018; das Chagas Silva, 2021). This work explores two schemes for the construction of gradients for the viscous flux calculation at volume faces.

Firstly, the cell-averaged gradients are computed by the Green-Gauss theorem, which can be written as

$$\left(\frac{\partial \phi}{\partial x}\right)_i = \frac{1}{V_i}\int_{V_i} \frac{\partial \phi}{\partial x} dV = \frac{1}{V_i}\int_{S_i} \phi \hat{n}_x \cdot dS \ , \tag{13}$$

where ϕ is a property of an i-th volume, $\hat{n}_x$ is the component in the x direction of the outward unit normal vector, V_i is the cell volume and S_i is the external face area. The first scheme to extrapolate the gradients at the cell faces is a volume weighted averaging (Jalali *et al.*, 2014). This method is named here as V00 and is given as

$$\left(\nabla \phi\right)_f = \frac{1}{V_i + V_j}\left(V_i \nabla \phi_i + V_j \nabla \phi_j\right) \ , \tag{14}$$

where the f, i, and j subscripts represent the f-th interface between two volumes, the cell to the left and the cell to the right of the interface, respectively. The second scheme is based on the work of Cary *et al.* (2009) and on the reference book by Blazek (2015), named here as V0E. This method modifies the projection of the face gradient towards the vector that links the cell centers (das Chagas Silva, 2021), being written as

$$\left(\nabla \phi\right)_f = \left(\nabla \phi\right)_{V00} - \left[\left(\nabla \phi\right)_{V00} \cdot \frac{\vec{r}_k}{|\vec{r}_k|} - \frac{\phi_j - \phi_i}{|\vec{r}_k|}\right]\frac{\vec{r}_k}{|\vec{r}_k|} \ . \tag{15}$$

Here, $(\nabla \phi)_{V00}$ represents the gradient calculated by Eq. (14) and $\vec{r}_k$ is the distance between the cell centroids that share the same k-th face.

An implicit Euler scheme is employed to the time march and the linear system is solved by a symmetric Gauss-Seidel iterative method (Bigarella and Azevedo, 2009).

3. RESULTS AND DISCUSSION

In this section, the numerical results obtained with the BRU3D code are presented and discussed. The subsonic zero pressure gradient flat plate case is used for the solver verification. For flows that present complex physical phenomena, the transonic flow over the OAT15A airfoil and the high-lift flow over the McDonnell Douglas 30P30N multi-element airfoil are considered. Such cases are presented below.

3.1 Subsonic Zero Pressure Gradient Flat Plate

In this subsection, the verification of the computational tool is discussed. For this purpose, only the NLBSL-V2 turbulence model is used, computed with scheme V00, because the SST model was implemented and validated in previous work (Carvalho *et al.*, 2018) with quite a lot of success.

This case represents a turbulent flow over a zero pressure gradient flat plate. The studies of this test case use the numerical results reported by the NASA Langley Research Center through the Turbulence Modeling Resource (TMR) website (Rumsey, 2021) as reference. The documentation available includes boundary conditions, formulation of governing equations, meshes and numerical results obtained with some NASA codes. The flow conditions are specified in Tab. 1, where M_∞ represents the freestream Mach number, Re_L is the reference Reynolds numbers, L is a reference length, T is the temperature, α is the attack angle and μ_t/μ is the ratio between eddy viscosity and molecular viscosity coefficients at the freestream conditions.

Table 1: Flow conditions for the flat plate case.

M_∞	$\mathrm{Re_L}$	L [m]	T [K]	α [deg]	μ_t/μ
0.2	5x10^6	1.0	300	0.0	0.009

Here, the three more refined mesh levels, among the five meshes available in the TMR website, are used. So, the meshes here employed have 10024, 52689 and 208896 cells. The reference numerical results to evaluate the present calculations were obtained with the CFL3D NASA code (Rumsey, 2021), which is a structured cell-centered finite volume code, therefore appropriated for the present studies. All results from the CFL3D code here reported were obtained with the fine mesh, computed with the version of the SST turbulence model reported by Menter (1992), named in the TMR website as SST-Vm model. The TMR website does not provide any results with the nonlinear turbulence model or the SST version implemented in the BRU3D code. Considering that this study case has just the objective of verification of numerical tool, the comparison between these different turbulence models is consistent for this purpose.

Figure 1 shows, in a XY plane, the results for the contours of μ_t/μ for the three mesh levels used, in order to enable the visualization of μ_t production. The results of BRU3D code using the NLBSL-V2 model are compared with the CFL3D result, Fig. 1d. Assessing the results in Fig. 1a, 1b and 1c, it is seen that the solution is dependent of the mesh quality. The coarse mesh produced a large diffusion of μ_t production when comparing to the other meshes. When refining the mesh, the solution of the μ_t/μ field was better defined, closing in on the reference solution, Fig. 1d.

When comparing the BRU3D result in the fine mesh with the reference result, Figs. 1c and 1d, respectively, the CFL3D solution computed maximum values of μ_t/μ more upstream than the BRU3D solution, *i.e.*, from $x = 1.4$, and the thickness of region where there is significant production of μ_t is lower regarding the BRU3D result. This is expected because the definition of μ_t is not the same for the turbulence models used and the numerical formulations are different in each code. In addition to the governing equations being different, studies reported by other members of the research group, as by Oliveira and Azevedo (2019) and Oliveira and Azevedo (2020), indicate that the numerical parameters of the computational tool may produce significant effects in the final solution. Similarly, the form in which the viscous fluxes are calculated at cell interfaces can also lead to greater "spreading" of the μ_t contours, as observed in these results. With these considerations, the solutions presented have good agreement with the reference CFL3D result.

Figure 2 shows the velocity profiles at positions $x = 0.97008$ and $x = 1.90334$ of the flat plate, comparing them with the logarithmic law of the wall (Pope, 2000), given as

$$u^+ = \frac{1}{\kappa} \ln y^+ + B \,, \tag{16}$$

where κ is the von Kármán constant, $\kappa = 0.41$, and B is a constant given as $B = 5.0$. Observing Fig. 2, the turbulence model represents very well the viscous sublayer region, $y^+ < 5$. This is expected since the molecular viscosity is dominant, so the turbulence model should not influence the solution. In the viscous wall region, $y^+ < 50$, the molecular viscosity is still significant. In the log-law region, $y^+ > 30$, the boundary layer follow the logarithmic law. From $y^+ > 50$ the flow is fully turbulent. Therefore, the viscous effects are negligible and the total stress tensor has only the turbulent stress contribution, which are computed by the turbulence model. Based in the logarithmic law of the wall, the velocity profiles plotted in Fig. 2 show that the NLBSL-V2 model implementation was successful.

Both for the flat plate case and the other cases, the convergence criteria adopted are a drop of 4 orders of magnitude for the maximum density residue and aerodynamic coefficients stabilized. Figure 3 shows the convergence history for the flat plate case here discussed. The maximum residue, $\mathrm{RHS_{max}}^{(n)}$, was normalized by the residue of the first iteration, $\mathrm{RHS_{max}}^{(1)}$. Despite the convergence criteria having been reached, with lift and drag coefficients stabilized, the convergence history of the properties ρu, ρk and total energy per unit of volume were included in Fig. 3 to demonstrate the standard of code convergence, valid for the other cases too. The behavior of the ρk residue curve is different when compared to

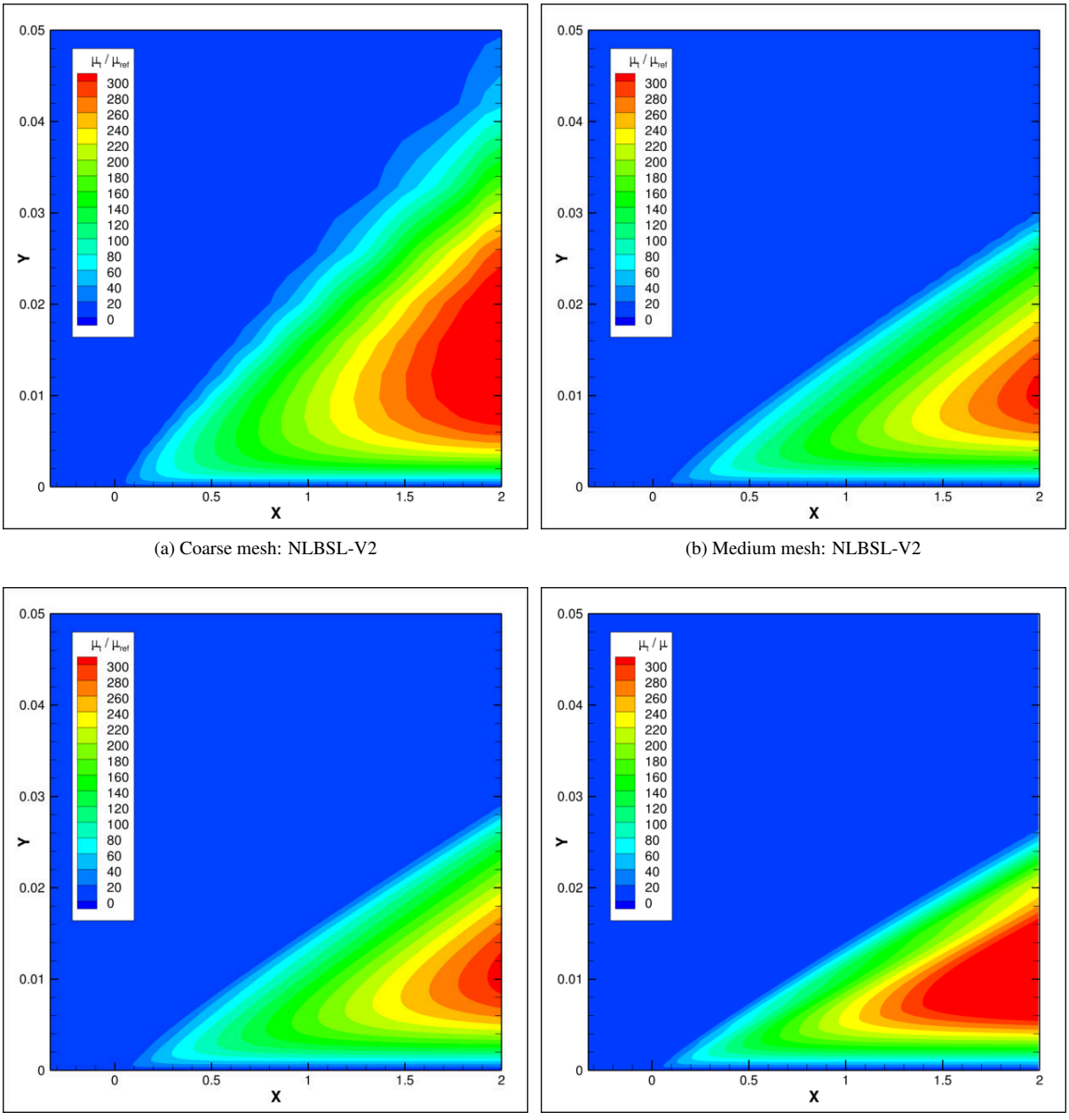

(a) Coarse mesh: NLBSL-V2

(b) Medium mesh: NLBSL-V2

(c) Fine mesh: NLBSL-V2

(d) Fine mesh: CFL3D

Figure 1: Contours of μ_t/μ for flat plate case obtained with the BRU3D code using NLBSL-V2 turbulence model and comparison with CFL3D code result using SST-Vm turbulence model.

the other variables, however, according to the research group experience, this behavior is standard to turbulent variables in codes that solve the RANS equations.

3.2 Transonic Flow over the OAT15A Airfoil

The transonic flow over the OAT15A airfoil was chosen to investigate anisotropy effects from the nonlinear turbulence model in the solution of a flow over a supercritical airfoil. The study of this case has three main goals, which are to evaluate the influences of grid refinement; for the most appropriate mesh, to analyze the effects of the nonlinear turbulence model; finally, to verify the influence of the use of different schemes in the viscous flux calculations in the solution of both turbulence models here employed. The major aerodynamic phenomena in this case are a shock wave on the upper surface of the airfoil and interaction between this shock and the boundary layer. This case has high-quality experimental results, reported by Roddle and Archambaud (1994) as case A-11. The flow conditions are shown in Tab. 2.

Firstly, three mesh levels are used, as shown in Fig. 4. All meshes consist of hexahedrals. The global refinement is 1.5 between each mesh level and 1.1 growth factor in the normal direction. These parameters were defined according to the

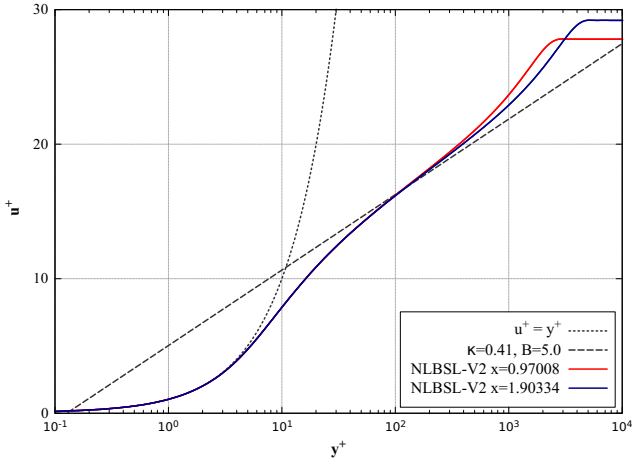

Figure 2: Comparison between the logarithmic law of the wall and velocity profiles obtained with the NLBSL-V2 turbulence model in two different points of the flat plate.

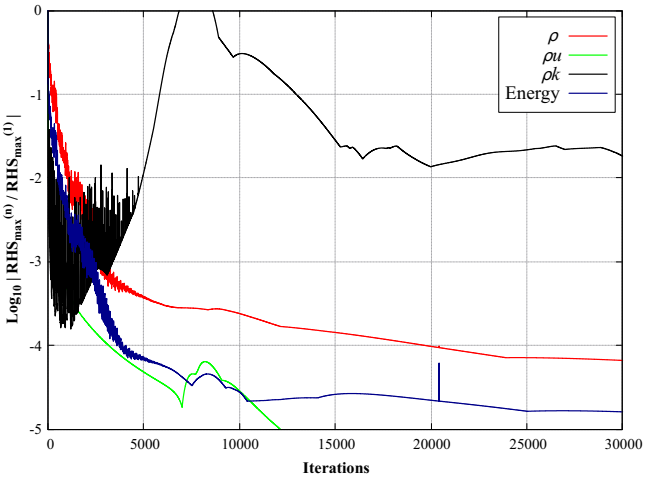

Figure 3: Residue curves from BRU3D code for the flat plate case with NLBSL-V2 turbulence model.

Table 2: Flow conditions for the OAT15A airfoil case.

M_∞	Re	c [m]	T [K]	α [deg]
0.724	3x10^6	1.0	246.66	1.15

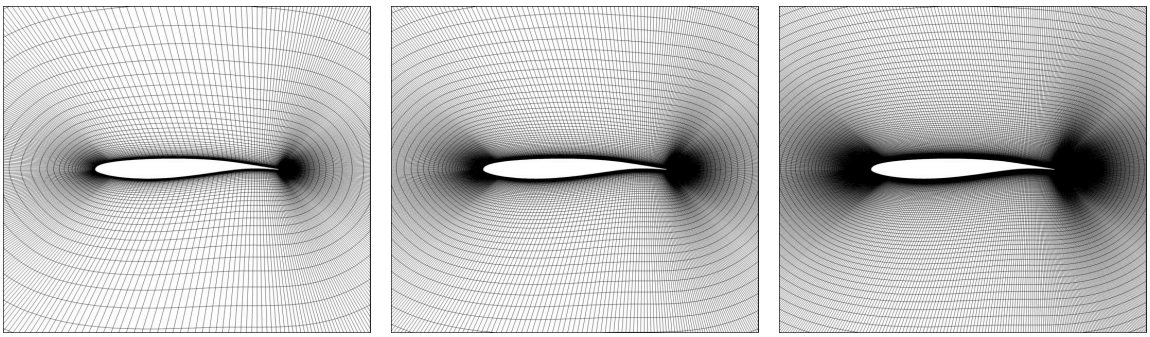

(a) Coarse mesh: 100x100 (b) Medium mesh: 150x150 (c) Fine mesh: 225x225

Figure 4: Overview of the meshes used in OAT15A airfoil case.

research group experience (Carvalho *et al.*, 2018). For this first objective of the study, only the V0E scheme was used.

In Table 3, the lift and drag coefficients, obtained with different turbulence models, are shown for each mesh level. All results were obtained with the V0E scheme and convergence criteria were satisfied. Looking at the lift coefficients, the variation in the values between medium and fine mesh levels for both turbulence models is insignificant, and the largest variation is about 0.15% for the NLBSL-V2 model. The same behavior can be observed for the drag coefficients, where the variations are 1.88% and 1.95% for SST and NLBSL-V2, respectively.

Table 3: Lift and drag coefficients for the OAT15A airfoil case obtained with V0E scheme.

Mesh Level	SST		NLBSL-V2	
	C_L	C_D (1)	C_L	C_D (1)
Coarse	0.69172	127.11	0.66506	122.12
Medium	0.69113	121.58	0.66243	116.51
Fine	0.69134	119.29	0.66143	114.24

(1) values in counts

Such results show that, with the mesh refinement made, mesh independence has not yet been reached. However, as changes in coefficient values are very small between medium and fine mesh levels, it was decided that the fine mesh is sufficiently refined to proceed with the other stages of this study case. An important point to be observed is that, regarding Tab. 3, depending on the turbulence model used, the solution seems to converge to different values. This is expected since the turbulence model effect is part of the solution. Experimental data are not available for this flow condition.

Figure 5 shows the pressure coefficient distributions over the OAT15A airfoil for the same cases shown in Tab. 3. Looking at the SST model curves, case (a), the solutions with the three mesh levels achieved almost the same results on the lower surface airfoil. However, there are a few differences with the experimental data. On the upper surface, the same behavior is observed, and even in the shock wave region, no significant change between mesh levels is seen. Similar considerations can be made for the NLBSL-V2 model results, case (b).

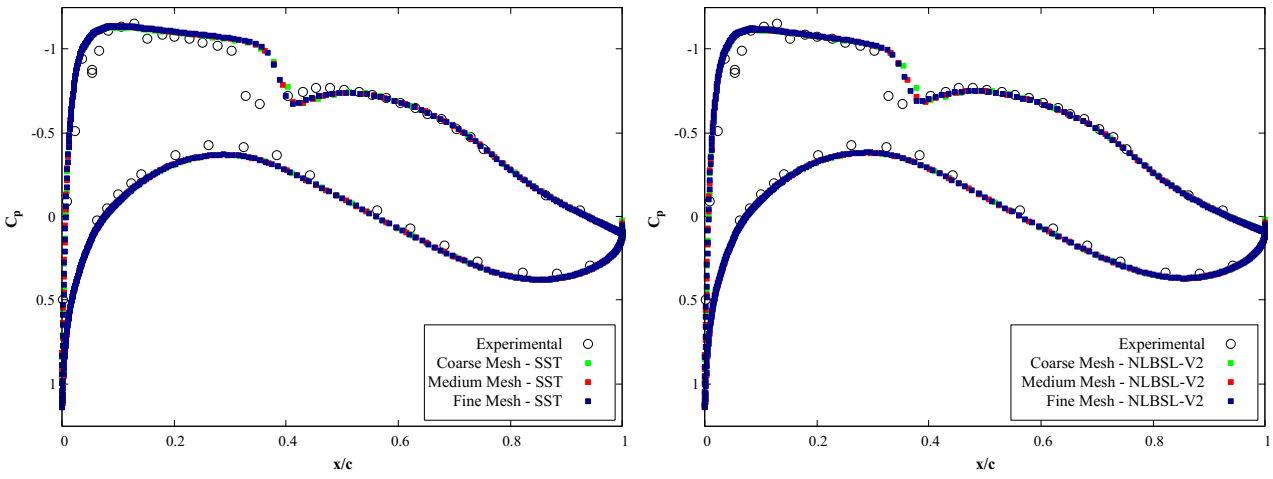

(a) SST Model (b) NLBSL-V2 Model

Figure 5: Pressure coefficient curves over OAT15A airfoil computed with V0E scheme.

Although no turbulence model has been able to capture the shock wave location with great accuracy, the shock wave position computed by the NLBSL-V2 turbulence model is closer to the experimental data. Case (a) in Fig. 6 shows the difference in solutions for each turbulence model obtained with one single viscous gradient scheme with the fine mesh. In this case, the improvement in the solution of the NLBSL-V2 model, the blue curve, is the result of an anisotropy formulation together with compressibility effects (das Chagas Silva, 2021). But, it is not just physical issues that can change a solution considerably. Now, the influence of the use of different schemes in the viscous flux calculations is analyzed using only the fine mesh.

Case (b) in Fig. 6 compares the pressure coefficient distribution over the OAT15A airfoil for each turbulence model computed with the V00 and V0E schemes. The shock waves obtained with the volume weighted averaging scheme, V00, for both turbulence models, yellow and light blue curves, are further downstream regarding the V0E scheme results. The modification that the V0E scheme proposes on the V00 scheme produced significant effects in solutions.

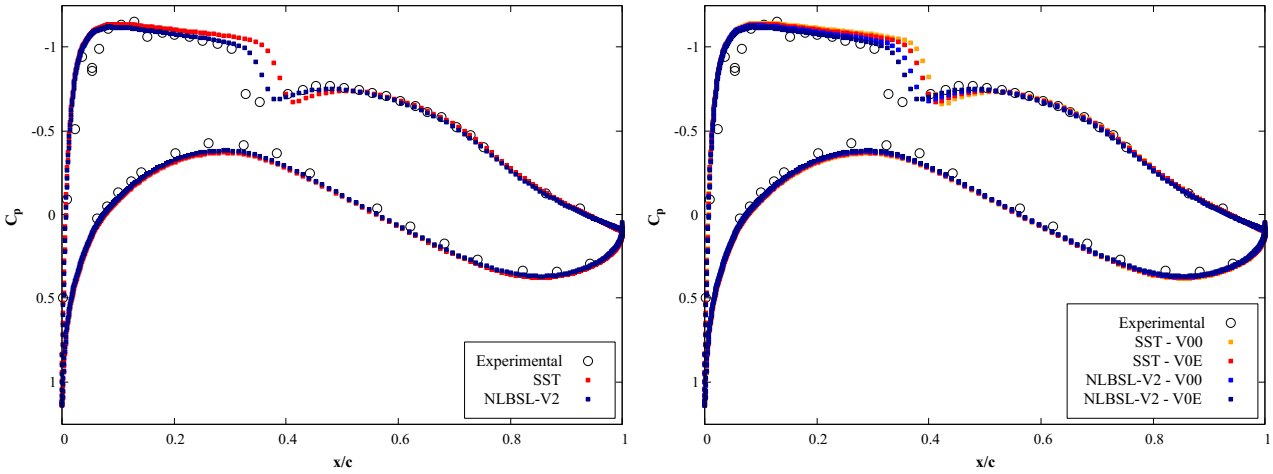

(a) Scheme V0E, only (b) Schemes V0E and V00

Figure 6: Pressure coefficient curves over OAT15A airfoil with fine mesh.

With the V0E scheme, the shock waves for both turbulence models are closer to the experimental location, in particular for the NLBSL-V2 model. It can be observed that the compressible effects present in this turbulence model have an effect very positive in the prediction of this case. However, the analysis of Fig. 6 demonstrates that the results are influenced by the numerical formulation implemented into the computational tool. For these results, it became evident that the error magnitude in the viscous flux calculations affects the solution. It is precisely this error that creates the differences between yellow and red curves, and between light blue and dark blue curves.

Figure 7 shows an enlarged view of the ρk contours on the shock wave region for each case, on the airfoil upper surface. The objective is to verify the effect of each viscous gradient calculation scheme on both turbulence models through the analysis of the ρk field. The dashed lines represent the region of the shock wave, which is positioned between 0.36 and 0.40% of the airfoil chord for the SST model and 0.34 and 0.38% for the NLBSL-V2 model.

When comparing the solutions with the same viscous flux calculation scheme, for different turbulence models, it is observed that the regions where there are significant levels of ρk are at different locations for each turbulence model. For example, in the SST solution, case (a), the region with higher levels of ρk is further downstream than in the NLBSL-V2 solution, case (b). This behavior is expected since they are different models, which means that the formulation of governing equations is different and this affects the solution directly. However, analyzing the results for the same turbulence model obtained with different viscous flux calculation schemes, for instance, cases (a) and (c), the same behavior happens. Moreover, in an even more pronounced way, because the regions with higher levels of ρk are even greater under this view than comparing different turbulence models with the same viscous gradient scheme. The same considerations are valid for nonlinear turbulence model results, NLBSL-V2.

As said, changes in solutions coming from changes in governing equations are expected. But, the changes in the solutions of Fig. 7 coming from numerical issues are fairly large and, considering that these changes are from purely numerical issues, they can be considered more significant than the changes in solutions between different turbulence models. Figure 8 illustrates the velocity profile of the turbulent boundary layer close to the trailing edge on the upper surface, at $x = 95\%$ airfoil chord. The velocity component U was made dimensionless by the freestream velocity. At this point along the airfoil upper surface, the boundary layer has already suffered the effects of its interaction with the shock wave and adverse pressure gradient.

It is verified that, for both turbulence models, the velocity profiles computed by the V00 scheme are more accelerated. The behavior seems to indicate that the V00 scheme calculates higher turbulence levels, resulting in a boundary layer more energized and stronger, consistent with the fact that shock waves from this scheme are further downstream than shock waves computed with the V0E scheme. However, the changes between curves of each case in Fig. 8 are due to purely numerical issues. Therefore, it shows how much the solution can be affected by numerical methods implemented into the code.

3.3 Flow over McDonnell Douglas 30P30N Multi-Element Airfoil

The second complex flow of this work aims to study high-lift aerodynamics. The main physical phenomena present in this type of flow are large pressure gradients and the interaction between boundary layers and wakes. Turbulence effects are strongly present in these phenomena. Accurate flow predictions allow for to reduce the interactions between boundary layers and wakes and between the boundary layer and pressure gradients of the mean flow, in order to optimize each device of the multi-element airfoil.

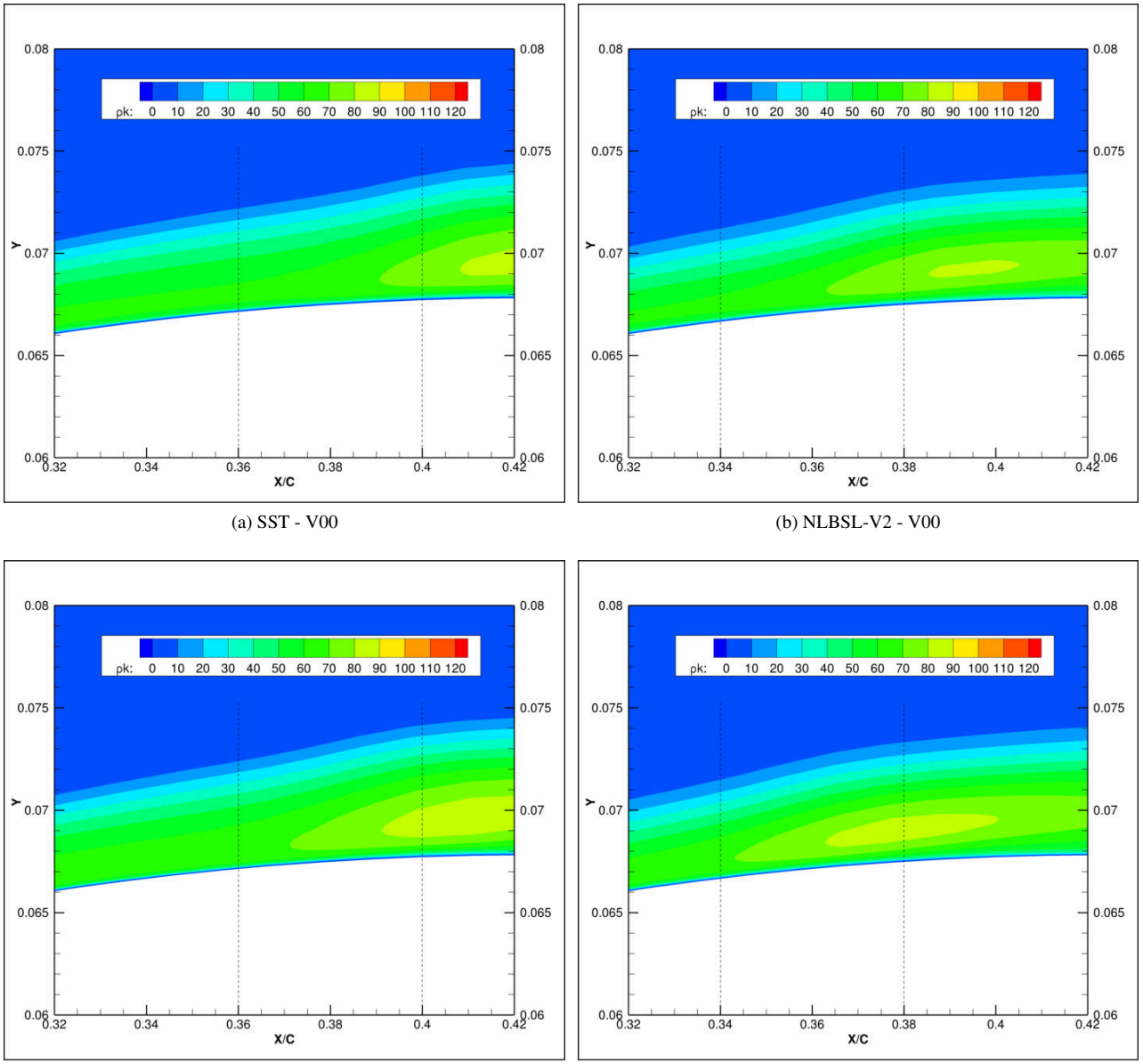

(a) SST - V00

(b) NLBSL-V2 - V00

(c) SST - V0E

(d) NLBSL-V2 - V0E

Figure 7: Enlarged view of turbulent kinetic energy contours in the shock wave region, on OAT15A airfoil upper surface, for comparison of the ρk field [J/m^3].

The two-dimensional flow over McDonnell Douglas 30P30N multi-element airfoil is the high-lift configuration chosen. The results obtained in this study are compared with experimental data (Chin *et al.*, 1993) realized by the Langley Research Center. The flow conditions are described in Tab. 4.

Table 4: Flow conditions for the 30P30N multi-element airfoil case.

M_∞	α [deg]	Re	c [m]	μ_t/μ
0.2	8	9x10^6	0.5588	3

Only one mesh is used in this study case, which is shown in Fig. 9. It consists of hexahedrals and the external boundary is located at 150 chords from the airfoil. The first mesh element has the recommended spacing, *i.e.*, $y^+ \leq 1$, on all airfoil surfaces, in order to ensure that turbulence models can be used under appropriate mesh refinement. Mesh details on the high-lift devices can be observed in Figs. 9b and 9c. The slat and flap deflections are -30 and 30 degrees, respectively.

The simulations are performed using the two turbulence models with different viscous flux gradient calculation

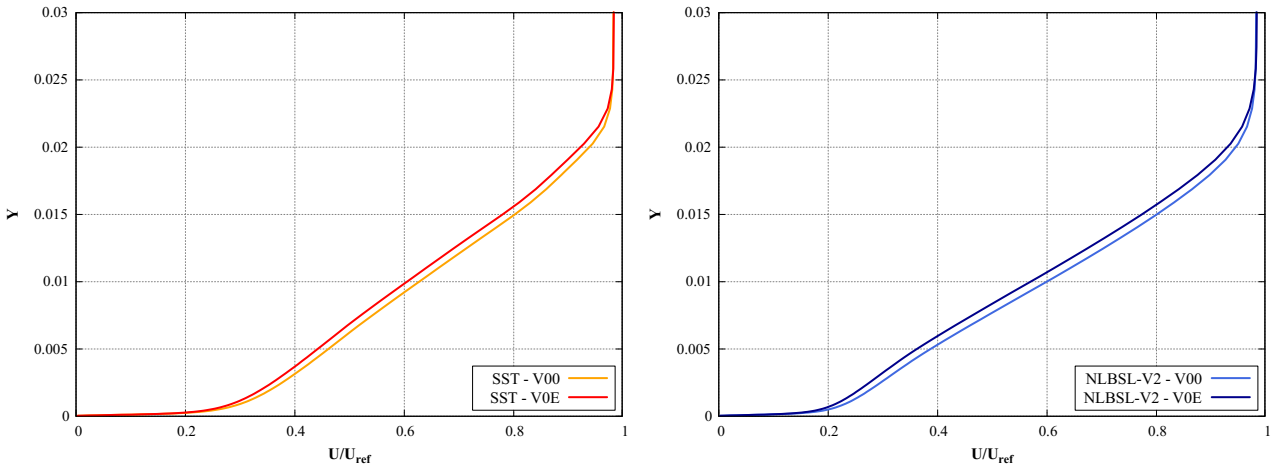

(a) SST (b) NLBSL-V2

Figure 8: Velocity profile at $x = 95\%$ of the OAT15A airfoil chord, on upper surface.

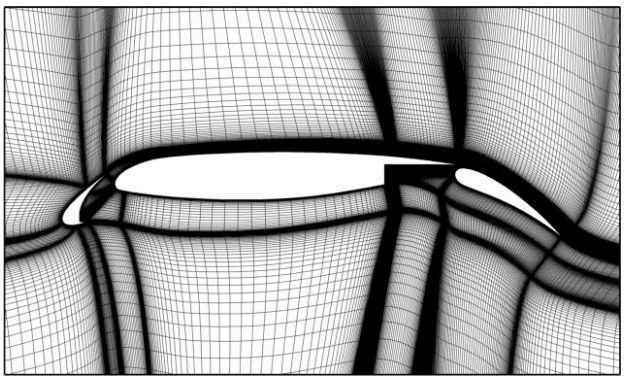

(a) Overview of the entire airfoil

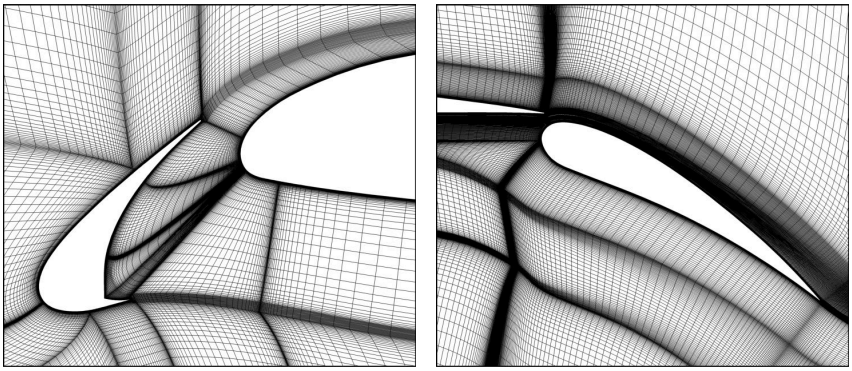

(b) Slat (c) Flap

Figure 9: Mesh over the McDonnell Douglas 30P30N multi-element airfoil with details of the high-lift devices.

schemes. Figure 10 shows the convergence history of the aerodynamic coefficients to compare the solutions of different turbulence models obtained with one single viscous gradient calculation scheme. The figures on the left side, Figs. 10a and 10c, represent the convergence curves of the lift coefficients for each gradient scheme. Similarly, the figures on the right side, Figs. 10b and 10d, represent the convergence curves of the drag coefficients. All the results presented in Fig. 10 were computed with the limiter function turned on.

Observing the SST solutions, which are represented by the red curves, it is seen that, for both aerodynamic coefficients, the values stabilize. This does not happen with the nonlinear turbulence model, blue curves. Although the lift coefficient results computed with the NLBSL-V2 model present variations, these are very small when compared to variations in the drag coefficient results. For the drag coefficients, such variations are around 60 and 70 drag counts for the solutions computed with the V00 and V0E schemes, respectively.

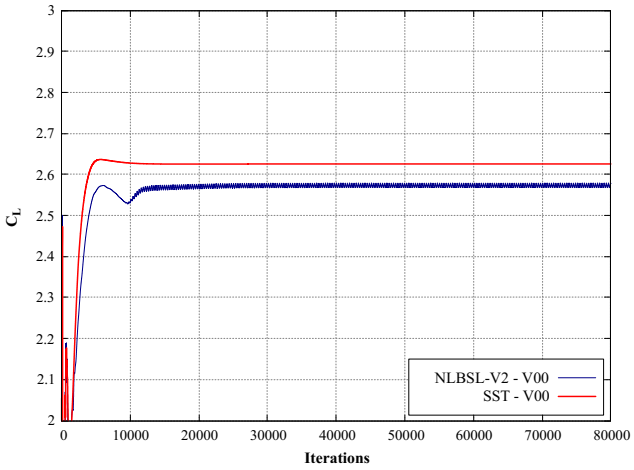

(a) C_L - Scheme V00

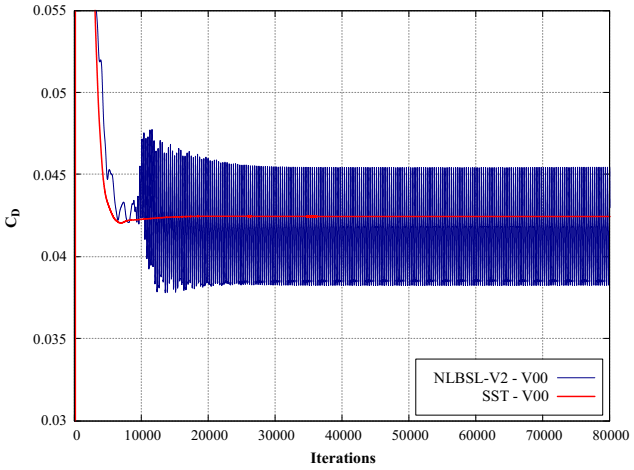

(b) C_D - Scheme V00

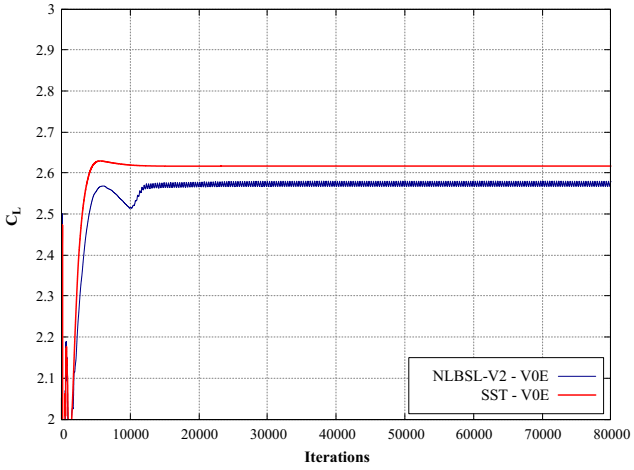

(c) C_L - Scheme V0E

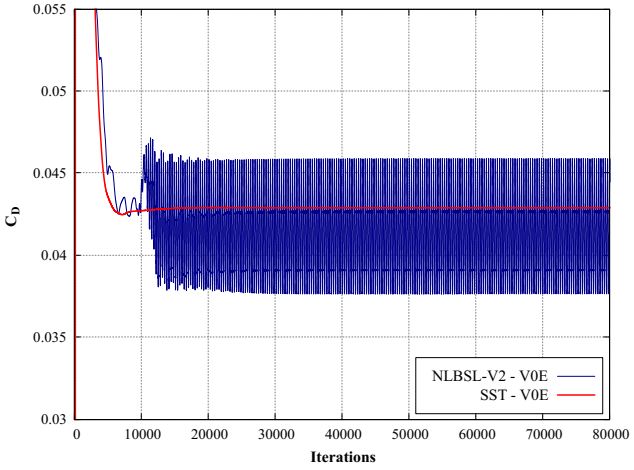

(d) C_D - Scheme V0E

Figure 10: Convergence of the aerodynamic coefficients, C_L and C_D, obtained with the two turbulence models with each viscous gradient calculation scheme for the 30P30N airfoil case.

The experimental values for lift and drag coefficients are 3.18 and 276 counts, respectively. There is some discrepancy between the experimental values and the numerical values computed with the SST model. Despite the NLBSL-V2 model not achieved the convergence criterion for the aerodynamic coefficients, it can be said that its mean values for both lift and drag coefficients also have differences regarding experimental data. Figure 11 shows the distribution of the pressure coefficient for the two turbulence models computed with one single gradient scheme. In general, the solutions for both schemes present good agreement with the experimental data.

One possible explanation for these results is that the aerodynamic coefficients obtained by the experimental method can have interference from the interaction between the flow with the wind tunnel walls, so that the effective angle of attack is greater than the nominal angle of attack indicated in the Tab. 4. This could result in an experimental value of lift coefficient greater than the computational result and, considering that the pressure values are measured in the middle of the test section, so, it would not have interference from the wind tunnel walls. This could explain the agreement of the simulations with the experimental pressure coefficient distribution and the disagreement with the experimental aerodynamic coefficient values.

However, Chin *et al.* (1993) says that the lift coefficient was calculated by integration of the pressure over the airfoil, *i.e.*, the same way as BRU3D code obtain the C_L values in its simulations. Thus, that should not be influenced by the wind tunnel walls in the experimental lift coefficient result. Based on this, no explanation was found for the divergence between the computation-experimental results of the lift coefficient. Regarding the drag coefficient, Chin *et al.* (1993) describes that the drag was not calculated from pressure distribution over the airfoil, but by the momentum deficit in the wake, also known as drag calculation in the far-field. As well as the lift coefficient, the BRU3D code calculates the drag coefficient by integrating the pressure over the airfoil, so, the difference in the way to calculate the C_D can have some effect in the final result.

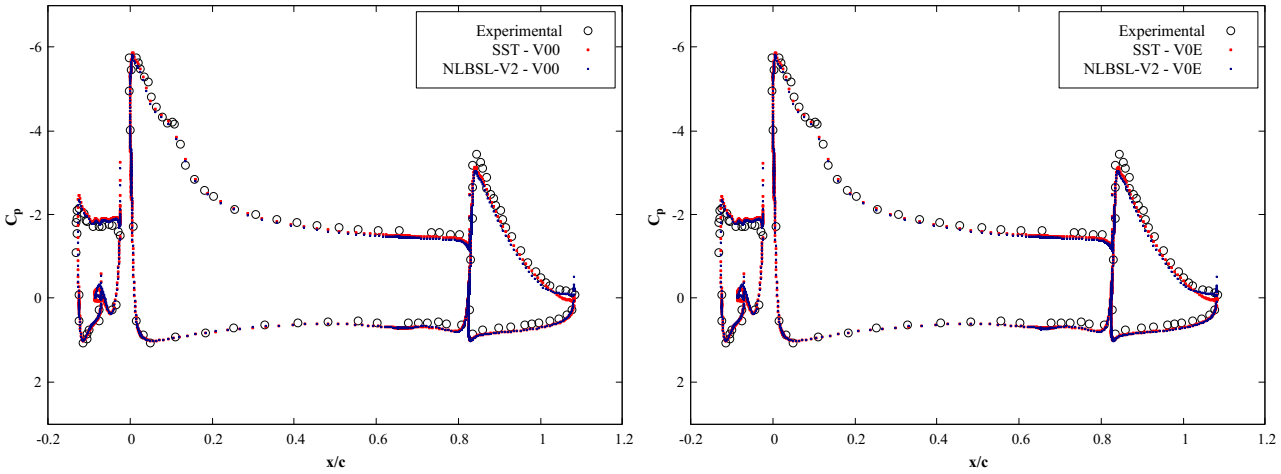

(a) Scheme V00 (b) Scheme V0E

Figure 11: Distribution of the pressure coefficient over 30P30N airfoil for the two turbulence models computed with each viscous gradient calculation scheme.

The analysis of the pressure coefficient distributions of the Fig. 11 shows that there are no significant variations both between the solutions of the turbulence models and between the solutions of the different viscous gradient calculation schemes. In general, for this case, the contribution of the nonlinear model could not be noted and the different gradient schemes did not produce significant distinctions between the final solutions. However, the study of these formulations in two-dimensional problems, both the different turbulence models and the different viscous gradient calculation schemes, is very important in order to, in the future, a next step be given with the use of these formulations in three-dimensional configurations. In such applications, it is expected that, at least, the anisotropy effects be most significant.

Based on the results obtained in Fig. 10, an investigation is made in order to identify the reason of the variations in the aerodynamic coefficients computed with the NLBSL-V2 model. The experiment of this flow condition (Chin *et al.*, 1993) reports that there is a separation of flow in the trailing edge region on the flap. Figure 12 shows the streamlines in this region for both turbulence models using the V0E scheme, which is the scheme that presents the greater variations in the drag coefficient values. The solution of the linear turbulence model, Fig. 12a, compute a separation further downstream that in the NLBSL-V2 solution, Fig. 12b. However, the presence of this physical phenomenon in the flow is not sufficient to determine if this study case is an unsteady problem.

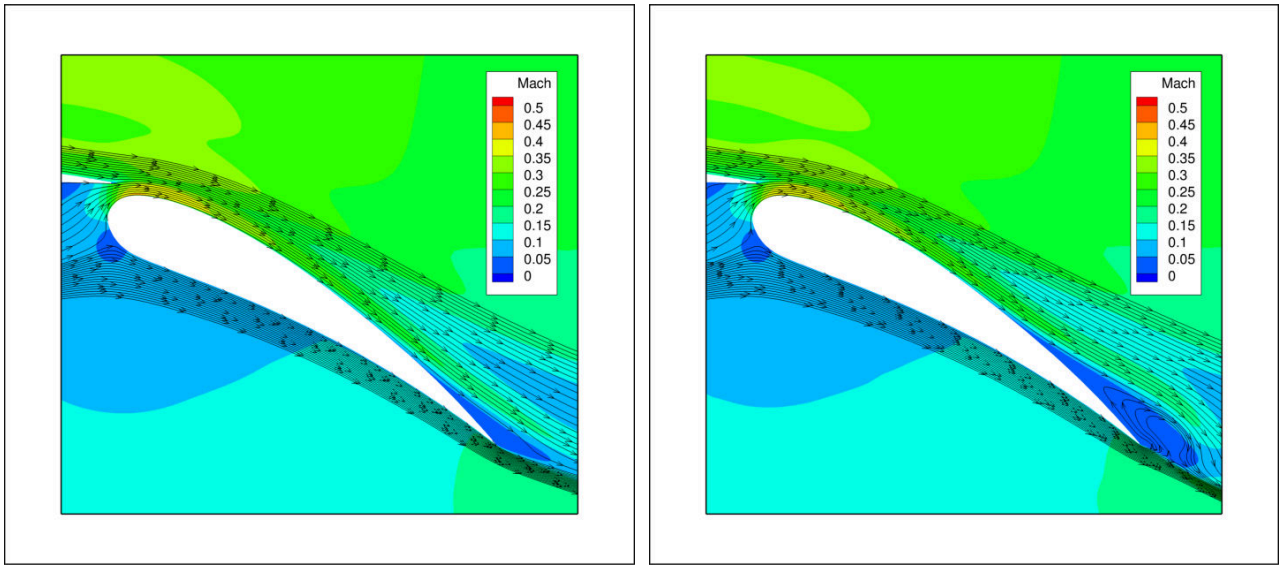

(a) SST Model (b) NLBSL-V2 Model

Figure 12: Streamlines in the trailing edge region on the flap of the 30P30N airfoil to observe the separation of flow. Results obtained with the scheme V0E.

Figure 13 presents the distributions of pressure coefficients for the NLBSL-V2 model obtained at the instants of iterations 50000, 60000, 70000 and 80000. The purpose of this analysis is to identify if there are significant changes in the pressure coefficient distributions between these iterations, which it could, in some way, explain the non-convergence of the aerodynamic coefficients computed with the nonlinear model, mainly the large variations of the drag coefficients. The slat and main surface of the airfoil are not shown because there are no significant changes in the pressure coefficient distributions or some physical phenomenon that could to take to non-convergence of the aerodynamic coefficients, like a separation of the flow caused by a weakness of the boundary layer, for example. Analyzing the Fig. 13, the differences in the pressure coefficient distributions on the trailing edge of the flap, for both gradient schemes, can not be considered large enough to cause changes around 60 counts in the drag coefficient, as shown in Fig. 10.

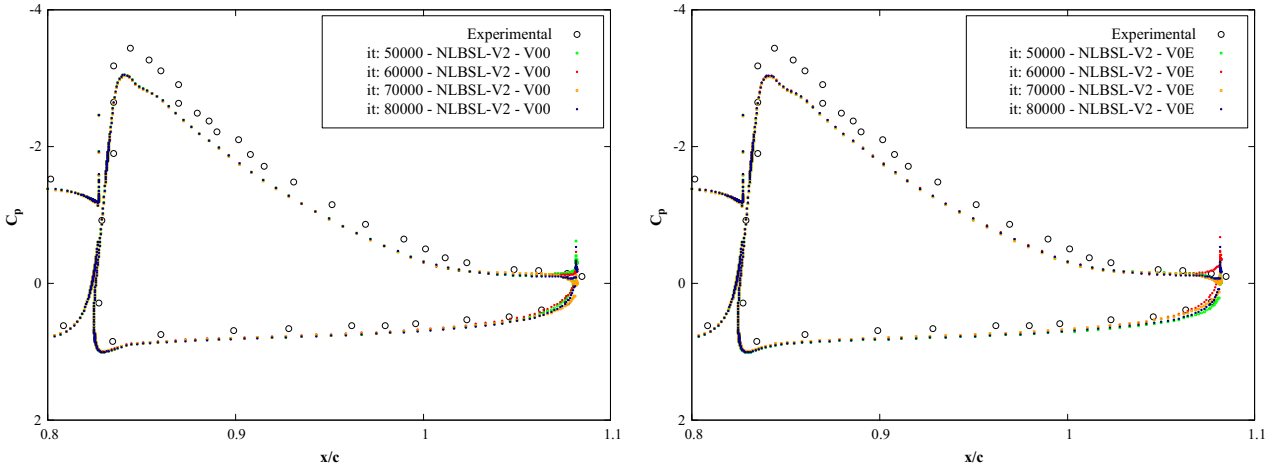

(a) Scheme V00 (b) Scheme V0E

Figure 13: Distributions of pressure coefficients on the flap of the 30P30N airfoil computed with the NLBSL-V2 model in different instants of iterations.

Like a last-ditch effort to identify the sources of the aerodynamic coefficient changes of Fig. 10, were made new simulations freezing the limiter function at iteration 10000. This means that, after of the iteration 10000, the limiter will work with the value calculated in the iteration 10000 until the end of the simulation. Figure 14 compares the convergence curves of the drag coefficients obtained by the NLBSL-V2 model with frozen limiter function at iteration 10000, blue curves, with the solutions computed with limiter function turned on during the entire simulation, green curves. For these results, regardless of the viscous gradient calculation scheme used, there is no evidence that the limiter function has any effect on the convergence of the drag coefficient computed with the NLBSL-V2 model. Although the amplitudes of the variations practically have not changed with the freezing of the limiter, the solutions are different. This is expected because the residue operator includes the limiter function.

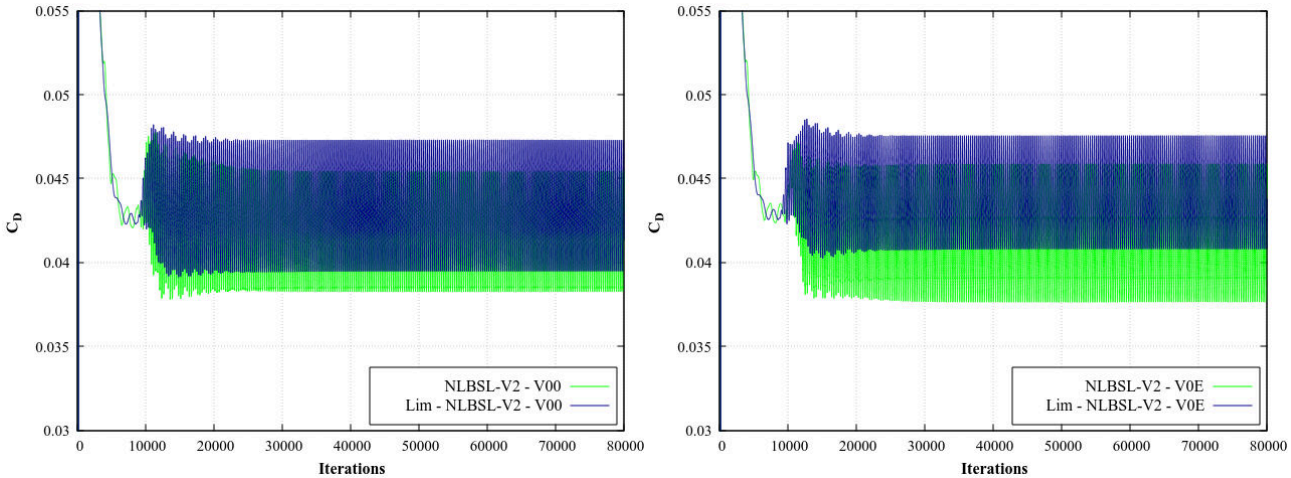

(a) Scheme V00 (b) Scheme V0E

Figure 14: Comparison between the convergence curves of the drag coefficients computed by the NLBSL-V2 model for the limiter on case during the entire simulation and frozen limiter at the iteration 10000.

Although the use of different gradient calculation schemes has had no significant effects in this case and the anisotropic contribution of the nonlinear turbulence model could not be observed, the lack of convergence of the aerodynamic coefficients shows that there are effects of the non-linearities present in this model. The drag coefficient results indicate that a steady-state solution is not being reached in these cases. However, the transient indicated in the variations in Fig. 14 is not a real transient, because, in order to obtain a steady-state solution, all solutions presented were computed with constant CFL. Such results indicate that perhaps it is not possible to achieve a steady-state solution with this nonlinear turbulence model. However, this is only an indication, a hypothesis. To make sure of this, it is necessary to perform the same simulations with a constant time-step, in order to reproduce a real transient, if it indeed exists.

It should also be observed that, although a mesh refinement study has not been performed in this case, the mesh used was generated with the best industry practices. Therefore, it seems to be an appropriate mesh for the problem. However, since the nonlinear turbulence models are not common in the daily industry, a mesh refinement is an interesting study to be done in the future to observe if the mesh has any influence in the lack of convergence of the aerodynamic coefficients for this case.

4. CONCLUDING REMARKS

In the present work, some studies were conducted in order to analyze the numerical influence of two different viscous flux gradient calculation schemes in aeronautical applications. One linear and one nonlinear turbulence models were used and a few of the prediction capabilities of these turbulence models were discussed. The study cases involved a turbulent flow over a subsonic zero pressure gradient flat plate, the transonic flow over the OAT15A airfoil and the high-lift flow over the McDonnell Douglas 30P30N multi-element airfoil. The results were compared with experimental data and numerical solutions.

The flat plate case was employed in a verification process of the computational tool. The solution of the μ_t/μ field has shown a strong dependence of the mesh refinement in the final result. For the fine mesh, the solution obtained had a good agreement with the reference numerical data and the velocity profiles analyzed in two distinct points of the plate presented a great agreement with the logarithmic law of the wall, thus concluding the verification exercise of the computational tool.

For the OAT15A airfoil case, the aerodynamic coefficient results show that mesh independence has not been reached, however, the changes in the coefficient values were considered very small to compromise the other stages of the work. In the analyses of the pressure coefficient distributions, no significant changes were seen between mesh levels. Considering only the fine mesh, the anisotropy present in the NLBSL-V2 model, together with compressibility effects, significantly improved the solution. However, it was seen that the numerical influence can also change the solution considerably. The shock waves obtained with the V0E scheme, for both turbulence models, are further upstream regarding the V00 scheme solution, which resulted in a good improvement in both solutions. Through a detailed analysis of the ρk field and velocity profiles, it can be seen that an accurate solution does not depend only of the physics included in the governing equations, but also of the numerical methods implemented in the computational tool. It became evident that the error magnitude in the viscous flux calculation affects the solution. None of the gradient schemes, together with the turbulence model used, was able to capture the shock wave location exactly.

The 30P30N airfoil case considered only one single mesh made according to the appropriate specifications for the solution of such problem. The nonlinear turbulence model did not reach an effectively converged solution, for both gradient schemes, because the aerodynamic coefficients did not completely stabilize along the iterative process. Despite this, one can be observe that there are differences in the flow topology, in particular, in the trailing edge region on the flap, where there is a flow separation, depending on the turbulence model adopted. No physical phenomenon that could indicate a possible source of non-stationarities in the solution was found in the flow. Studies also did not indicate the limiter function as the reason for such variations in the aerodynamic coefficients. Even without any significant noticeable effects in the use of different gradient schemes or in the anisotropic contribution of the nonlinear turbulence model, the non-convergence of the NLBSL-V2 model indicated that there are effects of the non-linearities present in this model. It was not possible to conclude if such turbulence model allows for a steady-state solution in this particular case. However, it was very interesting to identify the present behavior and it is something that deserves further investigation in order to complete the validation process of the model implemented.

In general, the numerical influence in the use of different viscous flux calculation schemes proved to be important to obtain an accurate final solution in turbulent flow represented by the RANS equations. This line of research should also study other methods, in order to improve the robustness of the computational tool for the applications of the interest. Faced with the non-convergence of the aerodynamic coefficients for the 30P30N airfoil case computed with the NLBSL-V2 model, it must be checked if this model allows a steady-state solution. Simulations with constant time-step may help in this investigation. This study case raised an important issue for the ongoing development of the solver, which is the need to use the limiter function in a case with Mach number relatively low. Under these conditions, the limiter should not be active. This is an aspect that certainly needs to be investigated by the research group. For the continuation of the validation of the nonlinear turbulence model, NLBSL-V2, is necessary to use it in cases in which the anisotropy effects are more significant, such as studies in which the flow is effectively three-dimensional.

5. ACKNOWLEDGEMENTS

The authors acknowledge the support for the present research provided by the computational resources from the Center for Mathematical Sciences Applied to Industry, CeMEAI, funded by Fundação de Amparo à Pesquisa do Estado de São Paulo, FAPESP, under the Research Grant No. 2013/07375-0. Further support to the 4th author under the FAPESP Grant No. 2013/07375-0 is also acknowledged. The authors also gratefully acknowledge the support for the present research provided by Conselho Nacional de Desenvolvimento Cientifico e Tecnologico, CNPq, under the Research Grant No. 309985/2013-7. This study was financed in part by Coordenação de Aperfeiçoamento de Pessoal de Nível Superior - Brasil (CAPES) - Finance Code 001.

6. REFERENCES

Barth, T.J. and Jespersen, D.C., 1989. "The design and application of upwind schemes on unstructured meshes". *27th AIAA Aerospace Sciences Meeting*, AIAA Paper No. 89-0366.

Bigarella, E.D.V. and Azevedo, J.L.F., 2005. "A study of convective flux computation schemes for aerodynamic flows". *43rd AIAA Aerospace Sciences Meeting and Exhibit*, AIAA Paper No. 2005-0633.

Bigarella, E.D.V. and Azevedo, J.L.F., 2009. "A unified implicit CFD approach for turbulent-flow aerospace-configuration simulations". *47th AIAA Aerospace Sciences Meeting Including The New Horizons Forum and Aerospace Exposition*, AIAA Paper No. 2009-1473.

Bigarella, E.D.V., 2007. *Advanced Turbulence Modeling for Complex Aerospace Applications*. Ph.D. thesis, Instituto Tecnológico de Aeronáutica, São José dos Campos, SP, Brazil.

Blazek, J., 2015. *Computational Fluid Dynamics: Principles and Applications*. Elsevier Ltd, Oxford, 3rd edition.

Carvalho, L.M.M.O., Almeida, A.C.V.M., da Silva, R.G., Basso, E. and Azevedo, J.L.F., 2018. "Robust parallel computations of turbulent aerodynamic flows". *2018 AIAA Aerospace Sciences Meeting*, AIAA Paper No. 2018-1788.

Cary, A.W., Dorgan, A.J. and Mani, M., 2009. "Towards accurate flow predictions using unstructured meshes". *19th AIAA Computational Fluid Dynamics*, AIAA Paper No. 2009-3650.

Chin, V.D., Peters, D.W., Spaid, F.W. and McGhee, R.J., 1993. "Flowfield measurements about a multi-element airfoil at high Reynolds numbers". *Proceedings of the 24th AIAA Fluid Dynamics Conference*, AIAA Paper No. 93-3137.

das Chagas Silva, T., 2021. *Modelos de Viscosidade Turbulenta Não Lineares para Simulações de Escoamentos Compressíveis em Aplicações Aeronáuticas*. Master Thesis, Instituto Tecnológico de Aeronáutica, São José dos Campos, SP, Brazil.

Hellsten, A., 2005. "New advanced k-ω turbulence model for high-lift aerodynamics". *AIAA Journal*, Vol. 43, No. 9, pp. 1857–1868.

Jalali, A., Sharbatdar, M. and Ollivier-Gooch, C., 2014. "Accuracy analysis of unstructured finite volume discretization schemes for diffusive fluxes". *Computers and Fluids*, Vol. 101, No. 2, pp. 220–231.

Menter, F.R., 1992. "Improved two-equation k-ω turbulence models for aerodynamic flows". *NASA TM 103975*.

Menter, F.R., 1994. "Two equation eddy-viscosity turbulence models for engineering applications". *AIAA Journal*, Vol. 32, No. 8, pp. 1598–1605.

Menter, F.R., Kuntz, M. and Langtry, R.B., 2003. "Ten years of industrial experience with the SST turbulence model". *4th International Symposium on Turbulence, Heat and Mass Transfer*, pp. 625–632.

Oliveira, F.B. and Azevedo, J.L.F., 2019. "Effects of numerical parameters and artificial dissipation in the simulation of inviscid nozzle flows". *25th ABCM International Congress of Mechanical Engineering*.

Oliveira, F.B. and Azevedo, J.L.F., 2020. "Effects of numerical parameters in the simulation of supersonic blunt body flows". *18th Brazilian Congress of Thermal Sciences and Engineering*.

Pope, S.B., 2000. *Turbulent Flows*. Cambridge University Press, New York, 1st edition.

Roddle, A.M. and Archambaud, J.P., 1994. "OAT15A airfoil data". In *A Selection of Experimental Test Cases for the Validation of CFD Codes, AGARD-AR-303*.

Roe, P.L., 1981. "Approximate Riemann solvers, parameter vectors, and difference schemes". *Journal of Computational Physics*, Vol. 43, pp. 357–372.

Rumsey, C., 2021. "Turbulence modeling resource web page". URL `<https://turbmodels.larc.nasa.gov/> Last access: Oct. 2021`.

van Leer, B., 1979. "Towards the ultimate conservative difference scheme. V. A second-order sequel to Godunov's method". *Journal of Computational Physics*, Vol. 32, No. 1, pp. 101–136.

Wallin, S. and Johansson, A.V., 2000. "An explicit algebraic Reynolds stress model for incompressible and compressible turbulent flows". *Journal of Fluid Mechanics*, Vol. 403, pp. 89–132.

7. RESPONSIBILITY NOTICE

The authors are solely responsible for the printed material included in this paper.